

03,13

## Memory effects and nonlinear electrical conductivity of doped perovskite-like lanthanum-strontium ferrite, $\text{La}_{0.5}\text{Sr}_{0.5}\text{Fe}_{0.75}\text{Al}_{0.2}\text{Ni}_{0.05}\text{O}_{3-\delta}$

© E.A. Petukhova, V.V. Kharton, V.V. Kveder

Institute of Solid State Physics, Russian Academy of Sciences, Chernogolovka, Moscow oblast, Russia

E-mail: elina.petukhova@issp.ac.ru

Received September 12, 2022

Revised September 12, 2022

Accepted September 24, 2022

Analysis of the existence of memory phenomena in model heterostructures based on doped ferrite  $\text{La}_{0.5}\text{Sr}_{0.5}\text{Fe}_{0.75}\text{Al}_{0.2}\text{Ni}_{0.05}\text{O}_{3-\delta}$  with a perovskite structure has been carried out. It was demonstrated that one 5–10  $\mu\text{m}$  thick ferrite layer sandwiched between Pt and Ni electrodes exhibits an analog memristor behavior. Under positive polarity, this heterostructure shows a smooth increase in electrical conductivity, with an opposite effect under negative polarity. Such phenomena are presumably associated with changing local concentrations of oxygen vacancies due to their drift in the electric field. Since lanthanum-strontium ferrites are sufficiently tolerant with respect to oxygen non-stoichiometry variations, no dendrite growth due to reductive decomposition is observed. The current vs. voltage dependencies display a strong nonlinearity resulting from the Poole–Frenkel effect, namely, a decrease in the activation energy of electron holes trapped on oxygen vacancies. In addition to the Poole–Frenkel effect, pre-exponential factor of the conductivity vs. temperature dependence also increases under electric field, indicating an increase in the effective electron-hole mobility.

**Keywords:** perovskite, lanthanum-strontium ferrites, memory effects, nonlinear electronic transport, memristors.

DOI: 10.21883/PSS.2023.01.54975.475

### 1. Introduction

Recent achievements in the field of „artificial intelligence“ and „deep machine learning“ based on artificial neural networks (ANN) have opened up ways to solve many problems that previously seemed insurmountable. Currently, ANN is usually implemented in the form of software in standard computers that only simulate neural networks. A radical increase in the efficiency of ANN can be achieved by creating special chips with a neuromorphic architecture [1–4], combining the storage and processing of information like neural networks in the brain of animals. To create artificial synapses in such chips, analog memristors are very attractive, i.e. electronic elements whose electrical resistance can change smoothly and reversibly depending on the charge flowing through them.

Currently, there are a huge number of publications devoted to the creation and research of memristors, and their number is growing rapidly. Most of the known memristors are based on thin films of metal oxides between two metal electrodes. There are at least two mechanisms that lead to a change in the electrical conductivity of these memristors when voltage is applied to them. One mechanism (the so-called analog memristors) is associated with a smooth change in electronic conductivity when the concentration of oxygen vacancies changes due to their drift in an applied strong electric field. The second mechanism (binary memristors having only two states) is based on the growth of very thin metal filaments due to „condensation“ of anion vacancies at a metal tip growing

from a negative electrode due to the vacancy drift in a strong local field near the tip [5,6]. When the growing metal thread touches the opposite electrode, there is a sharp decrease in electrical resistance — transition to the state „on“. The application of the opposite polarity leads to the dissolution of a part of the thread and a sharp increase in resistance — the „state is off“. Such memristors are quite suitable for binary non-volatile memory [7], but for synapses of neuromorphic networks, „analog“ memristors are much preferable.

Memristor effects have already been observed for many metal oxides ( $\text{TiO}_2$ ,  $\text{SiO}_2$ ,  $\text{CuO}$ ,  $\text{NiO}$ ,  $\text{CoO}$ ,  $\text{Fe}_2\text{O}_3$ ,  $\text{MoO}$ ,  $\text{VO}_2$ ) and oxide compounds, such as  $\text{SrTiO}_{3-\delta}$ ,  $(\text{La}, \text{Sr})\text{MnO}_3$ ,  $(\text{Pr}, \text{Ca})\text{MnO}_3$ ,  $\text{BaTiO}_3$ ,  $(\text{La}, \text{Sr})(\text{Co}, \text{Fe})\text{O}_3$  and  $\text{CeCu}_3\text{Ti}_4\text{O}_{12}$  [8–18]. Unfortunately, in most cases, a binary-type memristor effect was observed due to the almost inevitable formation of metal filaments or metal dendrites due to reactions like  $\text{Me}^{+2}\text{O}^{-2} + \text{V}_\text{O}^{+2} + 2e \Leftrightarrow \text{Me}^0$  occurring on a growing metal tip due to the drift of mobile oxygen vacancies ( $\text{V}_\text{O}^{+2}$ ). This system is unstable with respect to the growth of such metal dendrites and it is difficult to get rid of them. Analog memristors have been reported in only a few publications, including Pt/NiO/Ag [19] and Pt/ $\text{Co}_{0.2}\text{TiO}_{3.2}$ /ITO [20]. However, the analog behavior in the first case was unstable and the device easily switched to binary mode as a result of the formation of metal filaments. A more stable analog behavior has been reported for the Pt/ $\text{Hf}_x\text{Al}_{1-x}\text{O}_{1-y}$ /TiN [21] structure. In addition, both analog and binary characteristics in the

same device have been described in Ag-TiO films<sub>2</sub> [22], Ag/CH<sub>3</sub>-NH<sub>3</sub>PbI<sub>3</sub>Cl<sub>x</sub>/FTO [23] and Ni/Ta<sub>2</sub>O<sub>5</sub>/Si [24].

To obtain analog oxide memristors and avoid the appearance of metal filaments in them, it is desirable to use oxide compounds with the following properties:

- stability of the crystal lattice in a wide range of oxygen nonstoichiometry. The crystal structure of the oxide should be far from the structure of the corresponding metal;
- high concentration of oxygen vacancies and their sufficiently high mobility at room temperature;
- a large change in electronic conductivity with a change in the concentration of oxygen vacancies.

In this paper, we investigated the prospects of using perovskite-like lanthanum-strontium ferrites based on the La<sub>1-x</sub>Sr<sub>x</sub>FeO<sub>3-δ</sub> ( $x = 0-1$ ) oxide system for analog memristors.

Previously, this group of compounds (with various additional doping) was studied in detail as promising materials for the cathode layers of solid oxide fuel cells (SOFC) and oxygen membranes. It is known that when the strontium content is in the range  $x = 0.3-0.6$  and temperatures  $T > 600^\circ\text{C}$ , it combines a high oxygen diffusion coefficient and high electronic conductivity. These compounds belong to the structural type of perovskite ABO<sub>3</sub>, where La or Sr are at the positions *A* of the crystal lattice, and Fe (or dopant cations such as Al, Ni, Mo) occupy the *B* sites. Valence band and conduction band of La<sub>1-x</sub>Sr<sub>x</sub>FeO<sub>3-δ</sub> formed by overlapping wave functions of FeO<sub>6</sub> octahedra connected by corners. If there is no strontium ( $x = 0$ ) and oxygen vacancies ( $\delta = 0$ ) in the structure of La<sub>1-x</sub>Sr<sub>x</sub>FeO<sub>3-δ</sub>, iron ions have an average state Fe<sup>+3</sup> and the material is a wide-band semiconductor with a band gap of the order of 2.4 eV [25]. Replacement of the part of La<sup>3+</sup> with Sr<sup>+2</sup> leads to the appearance of holes in the valence band, which means that iron ions are partially in the Fe<sup>+4</sup> state. As strontium is added, the hole concentration increases, and the band gap width gradually drops to 1 eV [25]. In addition, the energy of formation of oxygen vacancies V<sup>+2</sup> decreases, which stimulates an increase in their concentration.

It is easy to understand that at a low temperature, the concentration of holes ( $p$ ) in the valence band should be  $p = x - 2\delta$  due to the crystal electroneutrality condition. Thus, an increase in the concentration of oxygen vacancies should lead to a drop in the concentration of holes in the valence band and a drop in  $p$ -type electronic conductivity. The disordered defect structure and the electron-phonon interaction (polaron effect) lead to partial localization of holes in the valence band (as for the Anderson dielectric aggravated by the polaron effect). Thus, the hole conductivity is essentially hopping in nature.

Such ferrites are characterized by relatively high thermodynamic and kinetic stability and a wide range of oxygen nonstoichiometry without phase transitions [26,27]. To increase the number of oxygen vacancies while maintaining high stability of the perovskite-like phase, we doped the base compound with aluminum and nickel cations.

Below we present the results of a study of the electrical conductivity of thin (about 5–10 μm) polycrystalline layers of perovskite La<sub>0.5</sub>Sr<sub>0.5</sub>Fe<sub>0.75</sub>Al<sub>0.2</sub>Ni<sub>0.05</sub>O<sub>3-δ</sub> in high electric fields in order to assess the prospects of using this group of materials to create analog memristors.

## 2. Samples and experimental procedures

Single-phase materials of the composition La<sub>0.5</sub>Sr<sub>0.5</sub>FeO<sub>3-δ</sub>, La<sub>0.5</sub>Sr<sub>0.5</sub>Fe<sub>0.8</sub>Al<sub>0.2</sub>O<sub>3-δ</sub> and La<sub>0.5</sub>Sr<sub>0.5</sub>Fe<sub>0.75</sub>Al<sub>0.2</sub>Ni<sub>0.05</sub>O<sub>3-δ</sub> were synthesized using the glycine-nitrate method [28,29]. The powders obtained during synthesis were annealed in an air atmosphere at a temperature of  $T = 1373$  K for 10 h, and then ground in ethanol in a ball mill with balls of zirconium dioxide with a diameter of 0.5 and 0.3 mm. The average particle size determined by the results of scanning electron microscopy (SEM, Supra 50 VP, Carl Zeiss) was equal to  $400 \pm 170$  nm.

To measure the temperature dependence of the specific electrical conductivity, ceramic samples were made in the form of cylindrical plates with a radius of 8.5 mm and a thickness of 1 mm by pressing the powders and sintering in air at 1673 K during 4 h. The specific electrical conductivity of these samples was measured by a standard four-point method with platinum contacts in the mode of slow cooling of the samples in a stream of dry argon or air.

Thin ceramic layers for measuring electrical conductivity in large electric fields were made by screen printing. The screen printing pastes were prepared by mixing the obtained powders in a ratio of 1:0.8 with an organic binder consisting of 10% polyvinyl butyral (Butvar B-98 Across Organics, USA) and 90% alpha-terpeniol (Shanghai Huizhong Technology, China).

The single-phase nature of the samples was checked using X-ray phase analysis on a Siemens D500 diffractometer (CuK<sub>α1</sub>-radiation). Diffractograms of the powders and ceramics are shown in Fig. 1, *a* and *b*, respectively. Table 1 shows the lattice parameters for the above compositions.

To study the electrical conductivity in a high electric field, a layer of platinum paste (Heraeus, Germany) with a thickness of 2 μm was applied onto a substrate of zirconium dioxide stabilized with yttrium (YSZ) and annealed at a temperature of 1223 K during 1 h. Then, using screen printing, a layer of ferritic paste was applied onto this layer of platinum and annealed at a temperature of  $T = 1473$  K

**Table 1.** Unit cell parameters and density of La<sub>0.5</sub>Sr<sub>0.5</sub>FeO<sub>3-δ</sub>, La<sub>0.5</sub>Sr<sub>0.5</sub>Fe<sub>0.8</sub>Al<sub>0.2</sub>O<sub>3-δ</sub> and La<sub>0.5</sub>Sr<sub>0.5</sub>Fe<sub>0.75</sub>Al<sub>0.2</sub>Ni<sub>0.05</sub>O<sub>3-δ</sub> (space group R $\bar{3}$ c)

Parameter	$a$ , Å	$c$ , Å	$V$ , Å <sup>3</sup>	$\rho$ , g/cm <sup>3</sup>
La <sub>0.5</sub> Sr <sub>0.5</sub> FeO <sub>3-δ</sub>	5.514	13.419	353.3	6.12
La <sub>0.5</sub> Sr <sub>0.5</sub> Fe <sub>0.8</sub> Al <sub>0.2</sub> O <sub>3-δ</sub>	5.474	13.373	347.0	6.07
La <sub>0.5</sub> Sr <sub>0.5</sub> Fe <sub>0.75</sub> Al <sub>0.2</sub> Ni <sub>0.05</sub> O <sub>3-δ</sub>	5.480	13.395	348.4	6.05

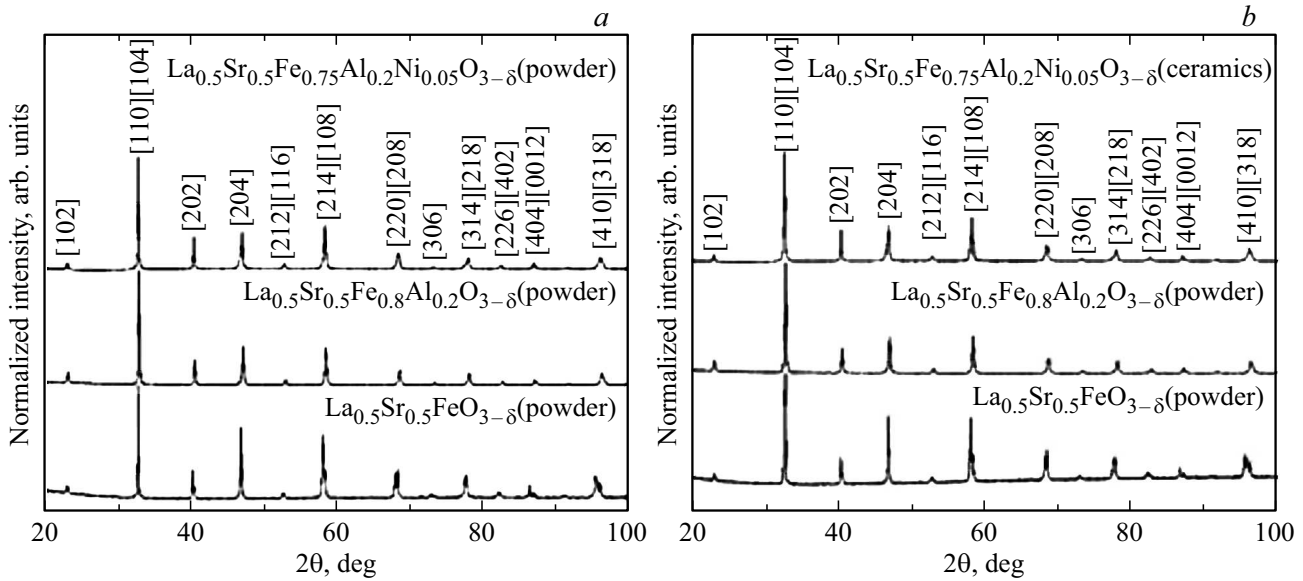


Figure 1. X-ray diffraction patterns of ferrite-based powders (a) and sintered ceramics (b).

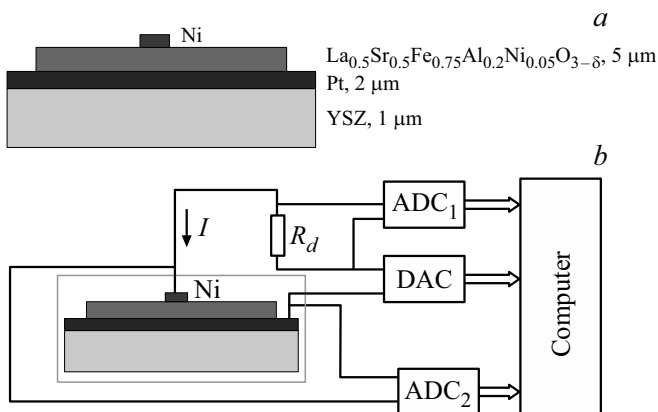


Figure 2. Schematic drawing of model heterostructures (a) and experimental setup for measuring electrical conductivity (b).

for 1 h in air. The thickness of the obtained layers was 5–10  $\mu\text{m}$ . A second contact, an electrode made of metallic nickel with a diameter of 0.5–0.7 mm was deposited onto the ferrite surface in vacuum (see Fig. 2, a).

The voltage to the heterostructure sample was applied using a digital-to-analog converter DAC through a series-connected constant resistance  $R_d$ , much lower than the resistance of the sample. The electrical conductivity  $S$  was calculated as  $S = I/U_b$ , where  $U_b$  — the voltage between the nickel and platinum contacts measured using an analog-to-digital converter ADC<sub>2</sub>, and  $I$  — the current which was calculated from the voltage drop at the resistance  $R_d$  measured using an analog-to-digital converter ADC<sub>1</sub>. To measure the differential (dynamic) electrical conductivity variations in the sample, in addition to a constant voltage, a small AC voltage was applied to it (using the DAC) at a

frequency of 30 Hz. The dynamic electrical conductivity  $S_d$  of the sample was calculated as  $S_d = \Delta I/\Delta U_b$ , where  $\Delta U_b$  and  $\Delta I$  — Fourier components of voltage and current at a frequency of 30 Hz, calculated by the computer from data collected from ADC<sub>2</sub> and ADC<sub>1</sub>.

### 3. Results and discussion

Figure 3 shows the temperature dependences of the electrical conductivity ( $\sigma$ ), measured during slow cooling of the ceramics in air (uncolored symbols) and in dry argon (painted symbols). The mechanism of the conductivity

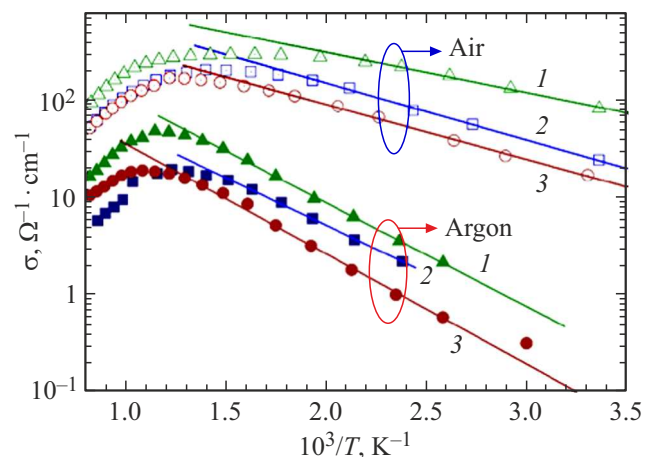
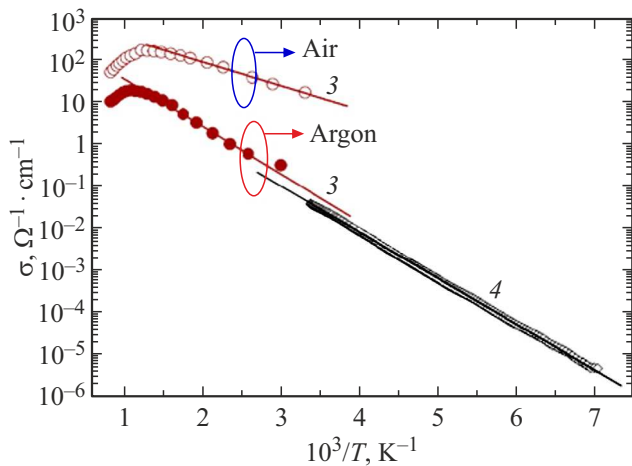


Figure 3. Temperature dependences of conductivity in Arrhenius coordinates,  $\log(\sigma)$  vs.  $1000/T$ , for  $\text{La}_{0.5}\text{Sr}_{0.5}\text{FeO}_{3-\delta}$  (1 — triangles),  $\text{La}_{0.5}\text{Sr}_{0.5}\text{Fe}_{0.8}\text{Al}_{0.2}\text{O}_{3-\delta}$  (2 — squares) and  $\text{La}_{0.5}\text{Sr}_{0.5}\text{Fe}_{0.75}\text{Al}_{0.2}\text{Ni}_{0.05}\text{O}_{3-\delta}$  (3 — circles) measured during slow cooling in flowing air (unfilled symbols) and in flowing dry argon (filled symbols).

**Table 2.** The values of the activation energy  $E_a$  and the pre-exponential factor  $\sigma_0$  calculated from the temperature dependence of the specific electrical conductivity at  $T < 500^\circ\text{C}$  when samples are cooled in air and in argon

Composition of the sample	In air	In dry argon
$\text{La}_{0.5}\text{Sr}_{0.5}\text{FeO}_{3-\delta}$	$E_a = 0.08 \pm 0.01 \text{ eV}$ , $\sigma_0 = 2053 \pm 3 \Omega^{-1} \text{ cm}^{-1}$	$E_a = 0.21 \pm 0.01 \text{ eV}$ , $\sigma_0 = 1163 \pm 3 \Omega^{-1} \text{ cm}^{-1}$
$\text{La}_{0.5}\text{Sr}_{0.5}\text{Fe}_{0.8}\text{Al}_{0.2}\text{O}_{3-\delta}$	$E_a = 0.12 \pm 0.02 \text{ eV}$ , $\sigma_0 = 2180 \pm 4 \Omega^{-1} \text{ cm}^{-1}$	$E_a = 0.19 \pm 0.01 \text{ eV}$ , $\sigma_0 = 454 \pm 3 \Omega^{-1} \text{ cm}^{-1}$
$\text{La}_{0.5}\text{Sr}_{0.5}\text{Fe}_{0.75}\text{Al}_{0.2}\text{Ni}_{0.05}\text{O}_{3-\delta}$	$E_a = 0.11 \pm 0.01 \text{ eV}$ , $\sigma_0 = 1188 \pm 3 \Omega^{-1} \text{ cm}^{-1}$	$E_a = 0.22 \pm 0.02 \text{ eV}$ , $\sigma_0 = 472 \pm 3 \Omega^{-1} \text{ cm}^{-1}$

**Figure 4.** Comparison of the conductivity of a thin layer  $\text{La}_{0.5}\text{Sr}_{0.5}\text{Fe}_{0.75}\text{Al}_{0.2}\text{Ni}_{0.05}\text{O}_{3-\delta}$ , thickness  $5 \mu\text{m}$ , deposited onto YSZ (without Pt layer) with the conductivity of bulk  $\text{La}_{0.5}\text{Sr}_{0.5}\text{Fe}_{0.75}\text{Al}_{0.2}\text{Ni}_{0.05}\text{O}_{3-\delta}$  ceramics in air (unpainted circles) and argon (painted circles).

variations in perovskite-like lanthanumstrontium ferrites was discussed elsewhere [26–38,30]. In general, the ionic contribution to the total electrical conductivity of such materials in this temperature range is negligible compared to the holes. The decrease in electrical conductivity with increasing temperature, observed in the high-temperature range,  $T > 600^\circ\text{C}$  ( $T > 833 \text{ K}$ ), occurs due to a progressive increase in the concentration of oxygen vacancies on heating, which leads to a decrease in the concentration of holes in the valence band and reducing their mobility. The same factor is responsible for the decrease in electrical conductivity when the sample is placed at a high temperature in an argon atmosphere compared to air.

At temperatures below  $T < 450^\circ\text{C}$  ( $T < 723 \text{ K}$ ), oxygen exchange between the sample and the atmosphere practically disappears, and the concentration of oxygen vacancies remains constant with a decrease in temperature. In this case, the temperature dependence of the electrical conductivity has a thermally activated character typical for semiconductors.

Table 2 shows the activation energy values ( $E_a$ ) calculated from the slope of the straight lines in Figure 3 corresponding to the dependencies:  $\sigma = \sigma_0^* \exp(-E_a/kT)$ .

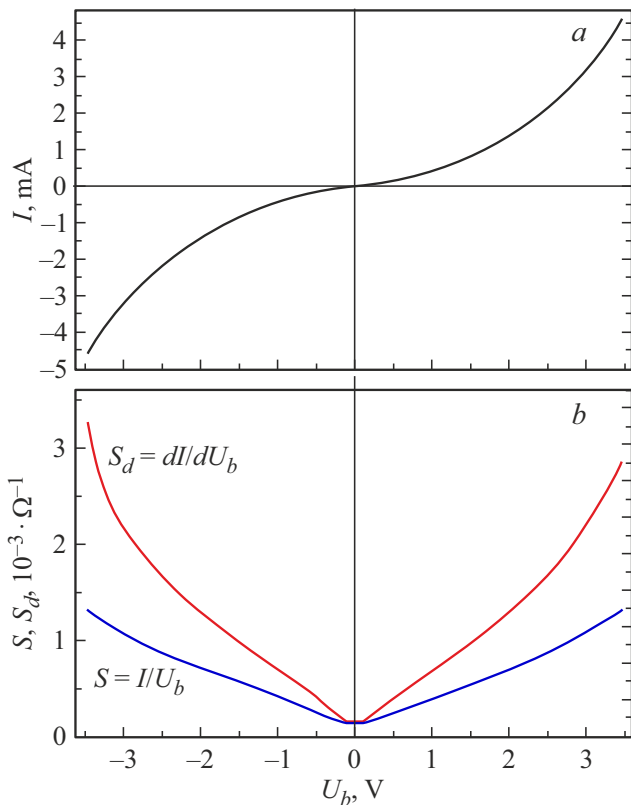
All experimental data given below correspond to samples of the composition  $\text{La}_{0.5}\text{Sr}_{0.5}\text{Fe}_{0.75}\text{Al}_{0.2}\text{Ni}_{0.05}\text{O}_{3-\delta}$ , characterized by the lowest conductivity in the studied series of materials.

Figure 4 compares the specific electrical conductivity of the layer  $\text{La}_{0.5}\text{Sr}_{0.5}\text{Fe}_{0.75}\text{Al}_{0.2}\text{Ni}_{0.05}\text{O}_{3-\delta}$  with a thickness of  $5 \mu\text{m}$  deposited onto a YSZ substrate without a Pt sublayer and rapidly cooled (quenched) after sintering at  $T = 950^\circ\text{C}$  ( $1223 \text{ K}$ ), and data on the bulk conductivity of ceramics from Fig. 3. The conductivity was measured along the layer using four Ni contacts. The results are in a good agreement with the bulk electrical conductivity of  $\text{La}_{0.5}\text{Sr}_{0.5}\text{Fe}_{0.75}\text{Al}_{0.2}\text{Ni}_{0.05}\text{O}_{3-\delta}$  measured on slow cooling in argon. The activation energy is  $0.21 \text{ eV}$ . The fact that  $E_a$  is constant over a wide temperature range indicates that there are no phase transitions and the conduction mechanism remains unchanged.

Figure 5 shows the dependence of the current  $I$ , as well as the static and dynamic electrical conductivity  $S = I/U_b$  and  $S_d = dI/dU_b$  on the voltage  $U_b$ , measured on the model heterostructure (see Fig. 2, a) Pt/ $\text{La}_{0.5}\text{Sr}_{0.5}\text{Fe}_{0.75}\text{Al}_{0.2}\text{Ni}_{0.05}\text{O}_{3-\delta}$ /Ni, in the fast scan mode ( $0.35 \text{ V/s}$ ) at  $T = 296 \text{ K}$ . It is clearly seen that the volt-ampere characteristics are highly nonlinear. There is no noticeable hysteresis when scanning rapidly up and down the voltage.

Figure 6 shows similar volt-ampere characteristics and dependences of static and dynamic electrical conductivity  $S = I/U_b$  and  $S_d = dI/dU_b$  on voltage  $U_b$ , for the same sample, but this time measured with dwells of 60 s at maximum positive and negative voltages. It is clearly seen that dwelling at  $U_b = +3.5 \text{ V}$  leads to an increase in electrical conductivity, whereas changing the polarity down to  $U_b = -3.5 \text{ V}$  leads to the restoration of the original characteristic.

It is essential that the increase and decrease in electrical conductivity occurs smoothly over time and the magnitude of the change can be controlled by changing the time of voltage application. This is illustrated in Fig. 7, which shows the kinetics of the process of „writing“ and „erasing“. At



**Figure 5.** Dependence of the current  $I$  on the voltage on the sample  $U_b$  for the model heterostructure Pt/La<sub>0.5</sub>Sr<sub>0.5</sub>Fe<sub>0.75</sub>Al<sub>0.2</sub>Ni<sub>0.05</sub>O<sub>3- $\delta$</sub> /Ni (a), and the conductivity dependencies  $S = I/U_b$  and  $S_d = dI/dU_b$  (b), measured in the fast scan mode (0.35 V/s).  $T = 296$  K.

time  $t = 0$ , a voltage of  $U_b = +4.8$  V was applied, which led to a monotonous increase in the electrical conductivity  $S = I/U_b$ , and at time  $t = 60$  s, a voltage of  $U_b = -4.8$  V, which caused a monotonic decrease in conductivity. Thus, we have „analog“ memristor effect.

It can be assumed that the nature of the observed hysteresis and the „memory“ effect is related to the redistribution of oxygen vacancies under the action of an applied electric field. Since the concentration of mobile charge carriers (electron holes in the valence band) is directly related to the concentration of oxygen vacancies, their redistribution leads to changes in conductivity. The observed lack of symmetry relative to the sign of the electric field is probably due to partial oxidation of the nickel electrode, which leads to a local increase in oxygen vacancies near it. Thus, the Ni electrode can probably act as a oxygen buffer. due to reversible oxidation and reduction of nickel interface. In addition, large characteristic switching times are also associated with a large sample thickness.

In order to shorten the characteristic transition time and increase the relative change in electrical conductivity during switching, we further plan to break the symmetry of the system not by using nickel, but by creating a

heterostructure of two layers with a different La/Sr ratio, which should lead to different concentrations of oxygen vacancies. According to our expectations, then switching will occur due to the redistribution of vacancies due to their drift between these layers. Moreover, in order to reduce

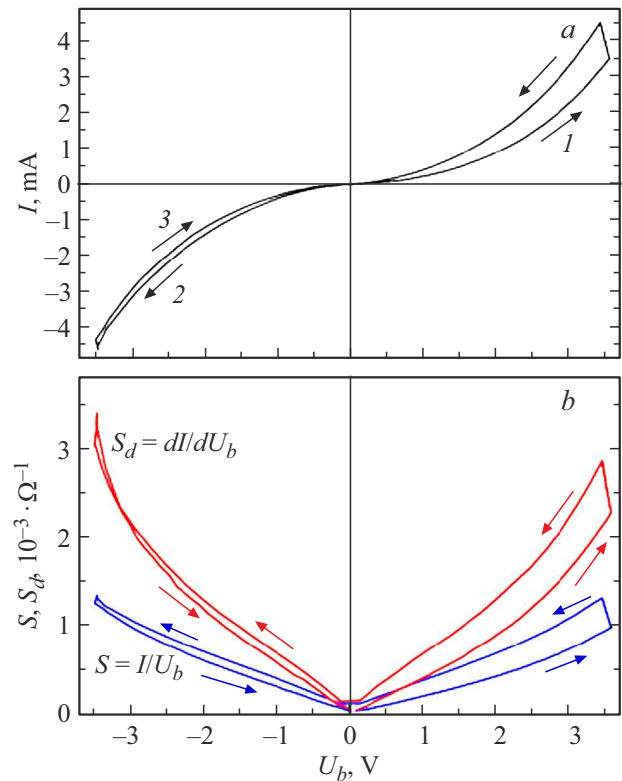


**Figure 6.** Dependence of the current  $I$  on  $U_b$  on the Pt/La sample <sub>0.5</sub>Sr<sub>0.5</sub>Fe<sub>0.75</sub>Al<sub>0.2</sub>Ni<sub>0.05</sub>O<sub>3- $\delta$</sub> /Ni (a), and the dependences of its electrical conductivity  $S = I/U_b$  and  $S_d = dI/dU_b$  (b), measured in the scanning mode  $U_b$  for 10 s from 0 to +3.5 V, then waiting 60 s at  $U_b = 3.5$  V, then 10 s scanning from +3.5 to -3.5 V, shutter speed 60 s and scan 10 s from -3.5 to 0 V,  $T = 296$  K.

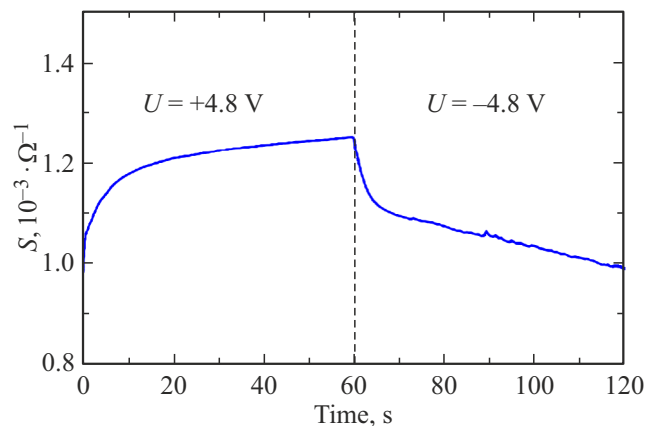


**Figure 7.** The dependence of the electrical conductivity  $S = I/U_b$  of the sample on time  $t$  when applied at the moment  $t = 0$  voltage +4.8 V, and at the moment  $t = 60$  s voltage -4.8 V.

the characteristic switching times, we plan to significantly reduce the thickness of the layers by using laser deposition.

In order to investigate the causes of the observed nonlinearity of the volt-ampere characteristics, we measured them at different temperatures using rapid voltage scanning in order to avoid the effects associated with the redistribution of oxygen vacancies. Figure 8 shows the temperature dependences of the conductivity  $S(T)$  of the tested heterostructure at various applied voltages  $U_b$ . The experimental data are well described by the dependencies  $S = S^* \exp(-E_a/kT)$ , shown in Fig. 8 by straight lines. Figure 9 shows the dependence of the activation energy  $E_a$  calculated from the slope of the straight lines in Figure 8 as a function of  $U_b^{1/2}$ . The experimental points fit well on the dependence  $E_a = 0.197 \text{ eV} + 0.0074 * U_b^{1/2} (\text{eV})$ , shown in Fig. 9 as a straight line.

The most likely reason for the decrease in the activation energy proportional to the square root of the electric field is the well-known Poole–Frenkel effect.

The Poole–Frenkel effect relates to reducing the energy of thermal activation of holes localized on traps (in our case, on oxygen vacancies) into the valence band under the influence of an external electric field  $\mathcal{E} = U_B/d$ , where  $d$  — the thickness of the sample ( $5\text{--}10 \mu\text{m}$ ). The Poole–Frenkel effect can often be observed for the defects with deep levels in semiconductors (see, for example, [31]). In the case of the Coulomb field around the defect  $U(r) = -e^2/\epsilon r$ , where  $e$  is the charge of the electron, and  $\epsilon$  is the effective permittivity, in the external field  $\mathcal{E}$  the energy of the hole captured by the defect can be expressed as

$$U(x) = -e^2/(x^* \epsilon) - e\mathcal{E}x, \quad (1)$$

where  $x$  is the distance in the direction of the field. The energy of thermal activation of the hole into the valence band is determined by the energy at the saddle point  $x = x_0$  of this potential corresponding to the zero derivative

$$dU/dx = e^2/(x_0^{2*} \epsilon) - \mathcal{E}e = 0. \quad (2)$$

It follows that  $x_0 = (e/(\mathcal{E}^* \epsilon))^{1/2}$ , and the reduction of the thermal activation energy by the electric field will be

$$\Delta E_a = U(\mathcal{E}) - U(0) = -e^*(e\mathcal{E}/\epsilon)^{1/2} = -\beta^*(U_b)^{1/2}. \quad (3)$$

The effective dielectric constant calculated from the capacitance of our sample measured at 1 MHz is equal to  $\epsilon \approx 4$ . Then for  $d = 5 \mu\text{m}$ , the value of  $\beta$  should be of the order

$$\beta = e^*(e/d\epsilon)^{1/2} \approx 0.0085 [\text{eV}^{1/2}]. \quad (4)$$

This estimate should also be valid for reducing the activation energy of jumping holes in a random Coulomb potential in the valence band associated with the random distribution of La and Sr ions in the  $A$  sublattice, as well as Fe, Al and Ni in the  $B$  perovskite sublattice. It is clear that the apparent activation energy for electrical conductivity is the sum of the activation energy for the hole concentration in the valence band and the activation energy for the hole diffusion.

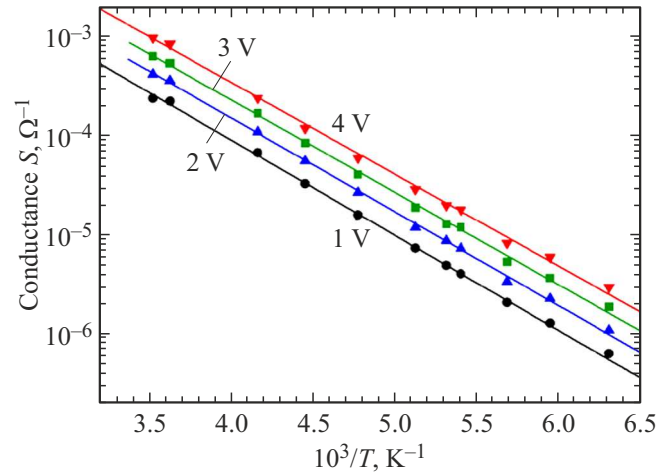


**Figure 8.** Dependences of the electrical conductivity of the sample on temperature in Arrhenius coordinates, measured at voltages  $U_b = 1, 2, 3$  and  $4 \text{ V}$ .

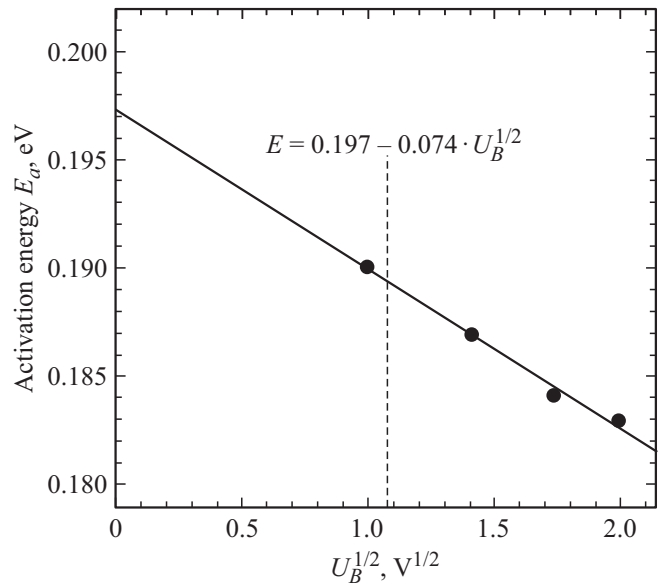


**Figure 9.** Activation energy calculated from the temperature dependence of electrical conductivity as a function of  $U_b^{1/2}$ .

As we can see, the experimental value of  $\beta = 0.0074 [\text{eV}^{1/2}]$  is sufficiently close to the calculated value of  $0.0085 [\text{eV}^{1/2}]$  which indicates that the Poole–Frenkel effect gives a noticeable contribution to the observed nonlinearity of electrical conductivity. Since  $S = S_0^* \exp(-E_a/kT)$ , a decrease in  $E_a$  with growing voltage  $U_b$  leads to a significant increase in electrical conductivity.

However, the Poole–Frenkel effect alone cannot fully explain the observed nonlinearity of electrical conductivity. This follows from Fig. 10, which shows the dependence of the value of the pre-exponential factor  $S_0$  on  $U_b$ , calculated from the data shown in Fig. 8.

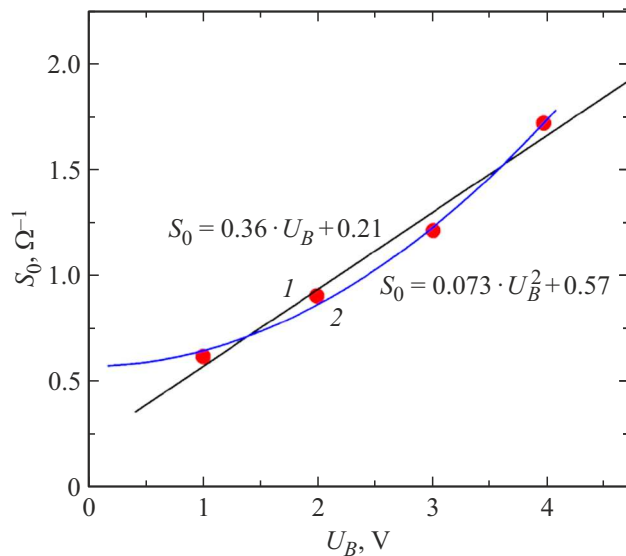


**Figure 10.** Dependence of  $S_0$  on  $U_b$ , where  $S_0$  — values of the pre-exponential factor calculated from the data in Fig. 8 for different values of  $U_b$ .

As can be seen from Fig. 10, the value of  $S_0$  increases very strongly with increasing voltage  $U_b$  and can be described as a linear dependence of  $S_0 = 0.21 + 0.36 \cdot U_b$ , or a quadratic dependence  $S_0 = 0.57 + 0.073 \cdot U_b^2$ .

The Poole–Frenkel effect does not imply the observed growth of  $S_0$  with an electric field. We believe that the electric field partially destroys the localization of holes in the valence band caused by local fluctuations of the composition. This leads to an increase in the effective mobility of holes and an increase of  $S$ .

#### 4. Conclusion

Electrical conductivity and memory effects in thin layers of perovskite-like lanthanum-strontium ferrite  $\text{La}_{0.5}\text{Sr}_{0.5}\text{Fe}_{0.75}\text{Al}_{0.2}\text{Ni}_{0.05}\text{O}_{3-\delta}$  were investigated for the first time. It was shown that model heterostructures comprising a single layer of  $\text{La}_{0.5}\text{Sr}_{0.5}\text{Fe}_{0.75}\text{Al}_{0.2}\text{Ni}_{0.05}\text{O}_{3-\delta}$  with a thickness of  $5\text{--}10\ \mu\text{m}$  sandwiched between the Pt and Ni electrodes demonstrate an analog memristor effect, i.e. a smooth reversible increase in electrical conductivity when an electric field of one polarity is applied and a decrease in electrical conductivity when an electric field of the opposite polarity is applied. We believe that the observed effect is due to a change in the local concentration of oxygen vacancies due to their drift in the electric field. The system proved to be stable with respect to the growth of metallic dendrites in the ferrite layer.

The strong nonlinearity of the current-voltage characteristics can be partially explained by a decrease in the thermal activation energy of holes trapped at oxygen vacancies due to the Poole–Frenkel effect, which leads to an increase in the concentration of holes in the valence band with an increase

in the electric field. In addition, the electric field leads to an increase in the pre-exponential factor of the temperature dependence of the electrical conductivity, which probably indicates an increase in the effective mobility of holes due to partial suppression of their localization. Thus, perovskites based on lanthanum-strontium ferrite can be considered as promising starting materials for analog memristors. In order to shorten the characteristic transition time and increase the relative change in electrical conductivity during switching, we further plan to break the symmetry of the system by removing Ni electrode and creating a heterostructure of two layers with different La/Sr ratios, which should lead to different concentrations of oxygen vacancies in them.

#### Funding

The work is partially supported by IFTT RAS — Russian government contracts. Electrical conductivity measurements were carried out within the framework of the project No. 17-79-30071, supported by the Russian Scientific Foundation.

#### Conflict of interest

The authors declare that they have no conflict of interest.

#### References

- [1] M. Prezioso, F. Merrikh-Bayat, B.D. Hoskins, G.C. Adam, K.K. Likharev, D.B. Strukov. *Nature* **521**, 7550, 61 (2015).
- [2] W. Zhang, B. Gao, J. Tang, P. Yao, S. Yu, M-F. Chang, H.-J. Yoo, H. Qian, H. Wu. *Nature Electronics* **3**, 7, 371 (2020).
- [3] M.A. Zidan, J.P. Strachan, W.D. Lu. *Nature Electronics* **1**, 1, 22 (2018).
- [4] B. Kim, S. Jo, W. Sun, H. Shin. *J. Nanosci. Nanotechnology* **19**, 10, 6703 (2019).
- [5] V.A. Chesnakov, V.V. Kveder. *Pis'ma v ZhETF* **58**, 210 (1993). (in Russian).
- [6] D. Xu, X.N. Shangguan, S.M. Wang, H.T. Cao, L.Y. Liang, H.L. Zhang, J.H. Gao, W.M. Long, J.R. Wang, F. Zhuge. *AIP Advances* **7**, 2, 025102 (2017).
- [7] O. Kavehei, A. Iqbal, Y.S. Kim, K. Eshraghian, S.F. Al-Sarawi, D. Abbott. *Proc. Royal Society A* **466**, 2120, 2175 (2010).
- [8] N.I. Mou, Y. Zhang, P. Pai, M. Tabib-Azar. *Solid-State Electron.* **127**, 20 (2017).
- [9] Z.-M. Liao, C. Hou, Q. Zhao, D.-S. Wang, Y.-D. Li, D.-P. Yu. *Small* **5**, 21, 2377 (2009).
- [10] F. Gul. *Ceram. Int.* **44**, 11417 (2018).
- [11] M.K. Rahmani, B.-D. Yang, H.W. Kim, H. Kim, M.H. Kang. *Semicond. Sci. Technol.* **36**, 095031 (2021).
- [12] G. Zhou, X. Yang, L. Xiao, B. Sun, A. Zhou. *Appl. Phys. Lett.* **114**, 163506 (2019).
- [13] L. JAMILPANAH, I. KHADAMI, J.S. GHAREHBAGH, S.A. MOHSENI, S.M. MOHSENI. *J. Alloys Comp.* **835**, 155291 (2020).
- [14] O.A. Novodvorsky, L.S. Parshina, A.A. Lotin, V.A. Mikhailovsky, O.D. Khramova, E.A. Cherebylo, V.Ya. Panchenko. *J. Surf. Investigat.: X-ray, Synchrotron Neutron Techniques* **12**, 2, 322 (2018).

- [15] R. Bruchhaus, R. Waser. *Thin Film Metal-Oxides*. Springer US, Boston, MA (2010). 131 c.
- [16] J.L.M. Rupp, P. Reinhard, D. Pergolesi, Th. Ryll, R. Tolke, E. Traversa. *Appl. Phys. Lett.* **100**, 012101 (2012).
- [17] Y.V. Pershin, M. Di Ventra. *Adv. Phys.* **60**, 145 (2011).
- [18] A.A. Felix, J.L.M. Rupp, J.A. Varela, M.O. Orlandi. *J. Appl. Phys.* **112**, 054512 (2012).
- [19] Y. Li, J. Chu, W. Duan, G. Cai, X. Fan, X. Wang, G. Wang, Y. Pei. *ACS Appl. Mater. Interfaces* **10**, 29, 24598 (2018).
- [20] M.M. Góis, M.A. Macêdo. *J. Mater. Sci.: Mater. Electron.* **31**, 5692 (2020).
- [21] A. Markeev, A. Choupruk, K. Egorov, Yu. Lebedinskii, A. Zenkevich, O. Orlov. *Microelectron. Eng.* **109**, 342 (2013).
- [22] X. Yan, J. Zhao, S. Liu, Zh. Zhou, Q. Liu, J. Chen, X.Y. Liu. *Adv. Functional Mater.* **28**, 1705320 (2018).
- [23] E. Yoo, M. Lyu, J.-H. Yun, Ch. Kang, Y. Choi, L. Wang. *J. Mater. Chem. C* **4**, (2016).
- [24] J.-H. Ryu, F. Hussain, Ch. Mahata, M. Ismail, Y. Abbas, M.-H. Kim, Ch. Choi, B.-G. Park, S. Kim. *Appl. Surf. Sci.* **529**, 147167 (2020).
- [25] L. Wang, Y. Du, P.V. Sushko, M.E. Bowden, K.A. Stoerzinger, S.M. Heald, M.D. Scafetta, T.C. Kaspar, S.A. Chambers. *Phys. Rev. Mater.* **3**, 025401 (2019).
- [26] V.V. Kharton, A.V. Kovalevsky, M.V. Patrakeev, E.V. Tsipis, A.P. Viskup, V.A. Kolotygin, A.A. Yaremchenko, A.L. Shaula, E.A. Kiselev, J.C. Waerenborgh. *Chem. Mater.* **20**, 20, 6457 (2008).
- [27] V.V. Kharton, J.C. Waerenborgh, A.P. Viskup, S.O. Yakovlev, M.V. Patrakeev, P. Gaczynski, I.P. Marozau, A.A. Yaremchenko, A.L. Shaula, V.V. Samakhval. *J. Solid State Chem.* **179**, 1273 (2006).
- [28] V.V. Kharton, M.V. Patrakeev, J.C. Waerenborgh, A.V. Kovalevsky, Y.V. Pivak, P. Gaczyński, A.A. Markov, A.A. Yaremchenko. *J. Phys. Chem. Solids* **68**, 355 (2007).
- [29] L.A. Chick, L.R. Pederson, G.D. Maupin, J.L. Bates, L.E. Thomas, G.J. Exarhos. *Mater. Lett.* **10**, 6 (1990).
- [30] E.V. Tsipis, E.A. Kiselev, V.A. Kolotygin, J.C. Waerenborgh, V.A. Cherepanov, V.V. Kharton. *Solid State Ionics* **179**, 2170 (2008).
- [31] O. Mitrofanov, M. Manfra. *J. Appl. Phys.* **95**, 11, 6414 (2004).